Pivot-and-bond model explains microtubule bundle formation

Marcel Prelogović[#1], Lora Winters[#2], Ana Milas[#3], Iva M. Tolić[*2,3], Nenad Pavin[*1]

[1] *Department of Physics, Faculty of Science, University of Zagreb, Bijenička cesta 32, 10000 Zagreb, Croatia*

[2] *Max Planck Institute of Molecular Cell Biology and Genetics, Pfotenhauerstr. 108, 01307 Dresden, Germany*

[3] *Division of Molecular Biology, Ruđer Bošković Institute, Bijenička cesta 54, 10000 Zagreb, Croatia*

(Received: 14 July 2017)

[#]These authors contributed equally to this work.

[*]Corresponding authors: N.P. (npavin@phy.hr) and I.M.T. (tolic@irb.hr).

ABSTRACT

During mitosis, bundles of microtubules form a spindle, but the physical mechanism of bundle formation is still not known. Here we show that random angular movement of microtubules around the spindle pole and forces exerted by passive cross-linking proteins are sufficient for the formation of stable microtubule bundles. We test these predictions by experiments in wild-type and *ase1*Δ fission yeast cells. In conclusion, the angular motion drives the alignment of microtubules, which in turn allows the cross-linking proteins to connect the microtubules into a stable bundle.

During mitosis the cell forms a spindle, a complex self-organized molecular machine composed of bundles of microtubules (MTs), which segregates the chromosomes into two daughter cells [1-3]. MTs are thin stiff filaments that typically extend in random directions from two spindle poles [4]. MTs that extend from the same pole can form parallel bundles, whereas MTs originating from opposite spindle poles form anti-parallel bundles [5-7]. Stability of MT bundles is ensured by cross-linking proteins, which bind along the MT lattice, connecting neighboring MTs. Cross-linking occurs only if the distance between the MTs is comparable with the size of a cross-linking protein. These proteins can be divided into two classes: (i) proteins that cross-link MTs without directed movement along the MT, such as Ase1/PRC1 (ref. [8]); (ii) motor proteins that walk along the MT either towards the plus end of the MT, such as Cut7/Eg5 (ref. [9,10]), or towards the minus end, such as Ncd (ref. [11,12]).

Spindle self-organization was studied in different biological systems and several theoretical models were proposed. Formation of antiparallel bundles of MTs in somatic cells of higher eukaryotes was investigated by computer simulations, which include MTs that grow in random directions from two spindle poles and motor proteins that link them [13]. Further, several studies have explored the forces generated in the antiparallel overlaps in vitro [14-16] and in *Drosophila* embryo [17-19]. Spindle formation was studied in *Xenopus* eggs, using the "slide and cluster" [20,21] and liquid crystal models [22,23]. In budding yeast, it is suggested that MTs growing in arbitrary directions from the opposite spindle poles can change their direction due to minus end directed kinesin-14 motors bound to both MTs and get aligned, forming anti-parallel bundles [24]. During spindle positioning, myosin motors walking along actin cables accelerate pivoting of astral MTs when they search for cortical anchor sites [25]. Studies in fission yeast have shown that passive (thermal) pivoting motion of MTs around the spindle pole body accelerates kinetochore capture [26-28], together with dynamic instability of MTs [29]. MT rotational motion about a pivot at the SPB was also included in the model for spindle formation [30] and in vitro studies [31]. However, observation of the dynamics of bundle formation in vivo and a corresponding physical model are required to understand the formation and stability of MT bundles.

In this paper, we combine experiments and theory to explore the formation of parallel MT bundles. We introduce the pivot-and-bond model for the formation of parallel MT bundles, which includes random angular motion of MTs around the spindle pole [26], along with the attractive forces exerted by cross-linking proteins. The model predicts faster bundle

formation if MTs diffuse faster and the density of cross-linking proteins is higher, which we tested experimentally. We conclude that the angular motion drives the alignment of MTs, which in turn allows the cross-linking proteins to connect the MTs into a stable bundle.

Experimentally observed bundle formation. The process of MT bundle formation can be observed experimentally in the fission yeast *Schizosaccharomyces pombe* because of a small number of MTs in the spindle. At the onset of mitosis, two spindle pole bodies nucleate MTs that form the spindle and additional MTs grow from the spindle pole bodies performing angular motion [26]. In our experiments, we observed that MTs growing at an angle with respect to the spindle eventually join the bundle of spindle MTs (Fig. 1a, Supplementary Movie 1 in ref. [32]). Such events are also accompanied by an increase in the tubulin-GFP signal intensity in the spindle, suggesting an increase in the number of MTs in the spindle and arguing against the scenario in which one of the MTs depolymerized (Fig. 1b). Additionally, we used cells with GFP-labeled Mal3, a protein that binds to the growing end of the MT [33]. Here we observed MT bundling at a finer time resolution (Fig. 1c, Supplementary Movie 2 in ref. [30]) and the increased Mal3 signal in the spindle after bundling (Fig. 1d). Aside from MTs joining the already formed spindle, we also observed bundling between pairs of MTs which were both freely pivoting (see Supplementary Figure 1a in ref. [30]). We did not observe un-bundling events after the bundles were formed. In all cases, MTs performed angular motion around the spindle pole body, which allowed them to approach each other and form a bundle.

Theory. To explore the physical principles underlying the formation and stability of MT bundles, we introduce the pivot-and-bond model (Fig. 2a). We describe two MTs as thin rigid rods of fixed length with one end freely joint at the spindle pole body, based on experimental observations both in vivo [26,27] and in vitro [34]. The orientation of the first MT at time t is described by a unit vector $\hat{\mathbf{r}}(t)$ (Fig. 2b). The orientation of the unit vector changes as

$$\frac{\mathrm{d}\hat{\mathbf{r}}}{\mathrm{d}t} = \boldsymbol{\omega} \times \hat{\mathbf{r}}, \tag{1}$$

where the vector $\boldsymbol{\omega}$ denotes angular velocity of the MT. The other MT has a fixed orientation along the z-axis in the direction of unit vector $\hat{\mathbf{z}}$. In the overdamped limit, the angular friction is balanced by the torque, $\mathbf{T}$, experienced by the MT:

$$\gamma\boldsymbol{\omega}=\mathbf{T}. \tag{2}$$

Here, γ denotes the angular drag coefficient. We calculate the total torque as $\mathbf{T}=\boldsymbol{\tau}+\sigma\left[\hat{\mathbf{r}}\times\boldsymbol{\eta}(t)\right]$, where the first and the second term represent the deterministic and the stochastic components, respectively. If the noise is caused by thermal fluctuations, as in fission yeast [26], $\boldsymbol{\eta}=(\eta_i)$, $i=1,2,3$ is a 3-dimensional Gaussian white noise, where i-th and j-th components for times t and t' obey $\langle\eta_i(t),\eta_j(t')\rangle=\delta(t-t')\delta_{ij}$, with $\delta(t-t')$ being the Dirac delta function and δ_{ij} is the Kronecker delta function. The magnitude of the noise is related to the angular drag coefficient, following the equipartition theorem, as $\sigma=\sqrt{2k_{\mathrm{B}}T\gamma}$, with $k_{\mathrm{B}}T$ being the Boltzmann constant multiplied by the temperature. We introduce the angular diffusion coefficient, $D=k_{\mathrm{B}}T/\gamma$, and the equation (2) now reads

$$\boldsymbol{\omega}=\frac{D}{k_BT}\boldsymbol{\tau}+\sqrt{2D}\hat{\mathbf{r}}\times\boldsymbol{\eta}(t). \tag{3}$$

In our model, the torque $\boldsymbol{\tau}$ in equation (3) is the consequence of forces exerted by cross-linking proteins connecting both MTs. If we denote the positions along the MTs as $\mathbf{r}=r\hat{\mathbf{r}}$ and $\mathbf{z}=z\hat{\mathbf{z}}$ respectively, the torque contribution from cross-linking proteins is

$$\mathrm{d}\boldsymbol{\tau}=\mathbf{r}\times\mathbf{f}\mathrm{d}N(r,z,t), \tag{4}$$

with $\mathrm{d}N$ being the number of cross-linking proteins connecting the MT elements $[z,z+\mathrm{d}z]$ and $[r,r+\mathrm{d}r]$. The force exerted by a single cross-linking protein is elastic and calculated as $\mathbf{f}=-k(\mathbf{y}-y_0\hat{\mathbf{y}})$. Here, k is the Hookean spring constant, $\mathbf{y}=\mathbf{z}-\mathbf{r}$ is the elongation of the protein linking positions $\mathbf{r}$ and $\mathbf{z}$, with magnitude y and direction $\hat{\mathbf{y}}=\mathbf{y}/y$, and y_0 is the relaxation length of the cross-linking protein. We describe the distribution of cross-linking proteins along the MTs by introducing the density, ρ, which obeys $\mathrm{d}N(r,z,t)=\rho(\mathrm{r},z,t)\mathrm{d}r\,\mathrm{d}z$. To calculate the total torque we summed up all the attached cross-linking proteins:

$$\boldsymbol{\tau}=k\int_0^R\mathrm{d}r\int_0^\infty\mathrm{d}z\rho\mathbf{r}\times\mathbf{z}\left(1-\frac{y_0}{y}\right), \tag{5}$$

where we used $\mathbf{r}\times(\mathbf{z}-\mathbf{r})=\mathbf{r}\times\mathbf{z}$ and allowed the fixed MT to span the entire positive z-axis. When the total number of cross-linking proteins is large we can use the mean field limit and consider them continually distributed along the MT. In this limit, the cross-linking protein density is given by:

$$\frac{\partial\rho}{\partial t}=-\frac{\partial j_r}{\partial r}-\frac{\partial j_z}{\partial z}+k_a c(r,z)-k_d(r,z)\rho. \tag{6}$$

Here, the currents describe the redistribution of cross-linking proteins along the MTs, $j_{\mathrm{r,z}}=v_{\mathrm{r,z}}\rho-D_{\mathrm{m}}\partial_{\mathrm{r,z}}\rho$, where the two terms correspond to the drift and the diffusion of cross-linking proteins, respectively. For passive cross-linkers, the velocities are calculated from the balance of the elastic force and friction of cross-linking proteins moving along the MT, $v_{\mathrm{r,z}}=f_{\mathrm{r,z}}/\gamma_{\mathrm{m}}$, where the components of the elastic force parallel with the corresponding MTs are calculated as $f_{\mathrm{r}}=\mathbf{f}\cdot\hat{\mathbf{r}}$ and $f_{\mathrm{z}}=-\mathbf{f}\cdot\hat{\mathbf{z}}$. The friction coefficient is calculated using the Einstein relationship, $\gamma_{\mathrm{m}}=k_{\mathrm{B}}T/D_{\mathrm{m}}$. We assume that the attachment rate k_{a} is constant and that the detachment rate depends on the force experienced by the cross-linking proteins [35], $k_{\mathrm{d}}(r,z)=k_{\mathrm{d0}}\exp\left[f\left(y(r,z)\right)/f_{\mathrm{c}}\right]$, with f_{c} being the critical force required for rupturing the MT-protein bond. The extensions of cross-linking proteins in the nucleoplasm are in thermodynamic equilibrium, hence they obey the Boltzmann distribution. Thus, the distribution of cross-linking proteins in the nucleoplasm with respect to their extensions is given by $c(r,z)=c_0\sqrt{k/2\pi k_{\mathrm{B}}T}\exp\left[-k\left(y(r,z)-y_0\right)^2/2k_{\mathrm{B}}T\right]$, where the constant c_0 is the linear concentration of cross-linkers in the nucleoplasm. Equations (1)-(6) provide a complete description of angular movement for the MT in the presence of cross-linking proteins.

To obtain the time course of the MT orientation, we parameterize the orientation of the MT given by the unit vector by $\hat{\mathbf{r}}(\theta,\varphi)=(\sin\theta\cos\varphi,\sin\theta\sin\varphi,\cos\theta)$, where θ and φ denote the polar and azimuthal angle, respectively. In this parameterization, the equation of motion for the polar angle reads

$$\frac{\mathrm{d}\theta}{\mathrm{d}t}=-D\frac{\partial U}{\partial\theta}+\sqrt{2D}\eta(t). \tag{7}$$

The normalized potential describing the interaction between the MTs, $U(\theta)$, is implicitly defined as $-\partial_\theta U=\tau/k_{\mathrm{B}}T+\cot\theta$, where τ denotes the magnitude of the torque and $\cot\theta$ is

the spurious drift term [36] (for derivation see Supplementary Note 1 in ref. [30]). This equation is sufficient to describe the bundling process, because the angle between the MTs is given only by the polar angle, the dynamics of which is independent of the azimuthal angle. In the adiabatic approximation, $\partial\rho/\partial t = 0$, equation (6) yields a one-dimensional cross-linker density profile $\rho_{\mathrm{r}}(r)$ (exact expression given by equation S21 in Supplementary Note 1, ref. [30]). Integrating the density profile over the entire length of the MT allows us to calculate the torque exerted by cross-linking proteins, which in turn allows us to calculate the generalized potential $U(\theta) = -\theta_{\max}\left[\Theta(\theta-\theta_{\min})/\theta + \Theta(\theta_{\min}-\theta)/\theta_{\min}\right] - \ln\left[\sin(\theta)\right]$. Here, $\theta_{\max} = k_{\mathrm{a}} c_0 y_0 / 4k_{\mathrm{d0}}$ is the local maximum of the potential, $\theta_{\min} = y_0/R$ is the local minimum and Θ is the Heaviside step function. The expression for the generalized potential combined with equation (7) formulates the pivot-and-bond model in terms of a one-dimensional Langevin equation.

By numerically solving equation (7) for the polar angle, for a large initial angle, we found that the MT performs random movement and spans a large space (Fig. 2c). However, the movement can become abruptly constrained in the vicinity of angle zero. These small angles correspond to a bundled state. Our numerical solutions also show that, in rare cases, constrained MT movement in the vicinity of angle zero can suddenly switch back to free random movement (Fig. 2d). The constrained movement near angle zero is a consequence of short range attractive forces exerted by the cross-linkers that accumulate in larger densities when MTs are in close proximity (compare green and magenta lines in Fig. 2e). The density is constant up to r_0 because in that region, the cross-linkers can always attach in a relaxed configuration, while for $r > r_0$, the cross-linkers will always be under tension and their density will drop off dramatically as r increases further (see illustration in Fig. 2e and Supplementary Note 1 in ref. [30]). Our numerically obtained time courses that correspond to the MT bundling are similar to those from experiments (compare Figs. 2c and 2f).

To systematically explore the formation of MT bundles and their stability, we first examine the normalized potential describing the interaction between the MTs. The shape of the normalized potential for different MT lengths and nucleoplasm cross-linker concentrations is shown in Fig. 3a. The normalized potential has a local maximum that introduces an intuitive boundary between two regions, $\Theta_{\mathrm{B}} \equiv [0, \theta_{\max}]$ and $\Theta_{\mathrm{u}} \equiv [\theta_{\max}, \pi]$, termed bundled and unbundled state, respectively. The bundling and unbundling probabilities are calculated as

$P_{\mathrm{B,U}} \propto \int_{\Theta_{\mathrm{B,U}}} \exp\left[-U(\theta)\right] \mathrm{d}\theta$, where we used the stationary probability distribution $\exp\left[-U(\theta)\right]$ and the normalization $P_{\mathrm{B}} + P_{\mathrm{U}} = 1$ (see ref. [36]). Bundling probability, shown in Fig. 3b as a function of cross-linker concentration, exhibits a sharp transition from zero to one around the value $P_{\mathrm{B}} = 1/2$. Based on this transition, we define bundles as stable if $P_{\mathrm{B}} > P_{\mathrm{U}}$. Thus, our theory predicts that stable bundles can form only if MTs are long enough and there are enough cross-linking proteins in the nucleoplasm (see Fig. 3c).

Finally, we calculate how the MT bundling time depends on the parameters of the system. In the case of an isotropic distribution of initial MT orientations, we calculate the bundling time as $\langle t_{\mathrm{B}} \rangle = (1/2D) \int_{\theta_{\min}}^{\pi} \langle t \rangle_{\theta,\theta_{\min}} \sin(\theta) \mathrm{d}\theta$, where $\langle t \rangle_{\theta,\theta_{\min}}$ is the first passage time from an initial angle θ to the angle $\theta_{\min}$ (for more details see Supplementary Note 1 in ref. [30]). After solving these integrals numerically, we found that the bundling time normalized by the diffusion coefficient, $\langle t_{\mathrm{B}} \rangle D$, decreases as the cross-linker concentration increases (solid black line in Fig. 3d), but is not significantly affected by the MT length (solid green line in Fig. 3d). Note that the bundling time, $\langle t_{\mathrm{B}} \rangle$, is inversely proportional to D, which decreases with MT length [26], thus we expect that the bundling time increases with MT length. The unbundling time, $\langle \mathrm{t}_{\mathrm{U}} \rangle$, is calculated analogously. The unbundling time becomes longer than bundling time if the condition for bundle stability $P_{\mathrm{B}} > P_{\mathrm{U}}$ is fulfilled. Once this condition is satisfied, the bundling time greatly increases (dashed line in Fig. 3d).

In order to compare the theory with experimental observations, we measured the bundling time as the total observation time of MTs divided by the number of observed bundling events, $\langle t_{\mathrm{B}} \rangle = t_{\exp}/n$ (see Supplementary Note 2 in ref. [30]). Along with the wild type cells, we also performed the measurements on the mutant in which the ase1 cross-linker was knocked out (denoted *ase*1Δ, ref. [37,38]), in which we also observed MT bundling (see Supplementary Figure 1b, Supplementary Movie 4, and Supplementary Table 1 in ref. [30]). We observed that the bundling time increases with MT length (Fig. 3e), and that the bundling time is significantly longer in *ase*1Δ cells (compare green and magenta line in Fig 3e). We normalized the bundling time by the diffusion constant and found a weak dependence on MT length, but a significant increase in *ase*1Δ cells compared to wild type (inset of Fig 3e, for theory see Supplementary Note 1, for diffusion measurements see Supplementary Figure 2, all

in ref. [30]). The theory reproduces the weak dependence on MT length and implies that the deletion of ase1 decreases the effective cross-linker concentration roughly five fold.

In conclusion, our work implies that only passive processes, thermally driven motion of the MTs and passive cross-linkers, are sufficient to describe the formation of parallel MT bundles. By introducing the pivot and bond model we gain a deeper understanding of the mesoscopic properties of the bundling process, such as bundle stability and average bundling time, as well as predict their dependence on biological parameters such as MT length and cross-linker concentration. This approach is complementary to more exhaustive and detailed methods such as large-scale numerical simulations (for example [30,39]).

Along with parallel MT bundles, mitotic spindles also contain bundles of anti-parallel MTs, which are made of MTs extending from the opposite spindle poles. The theory developed here could be generalized to describe MTs extending from two spindle poles by adding additional angular variables and including directional movement of cross-linking proteins. Just like here, such model will give insight into the minimal requirements for the formation of anti-parallel MT bundles and therefore shed additional light on the physics of spindle formation.

[1] A. Mogilner and E. Craig, *Towards a quantitative understanding of mitotic spindle assembly and mechanics*, J Cell Sci **123**, 3435 (2010).
[2] S. L. Prosser and L. Pelletier, *Mitotic spindle assembly in animal cells: a fine balancing act*, Nat Rev Mol Cell Biol **18**, 187 (2017).
[3] N. Pavin and I. M. Tolic, *Self-Organization and Forces in the Mitotic Spindle*, Annu Rev Biophys **45**, 279 (2016).
[4] M. Kirschner and T. Mitchison, *Beyond self-assembly: from microtubules to morphogenesis*, Cell **45**, 329 (1986).
[5] K. L. McDonald, E. T. O'Toole, D. N. Mastronarde, and J. R. McIntosh, *Kinetochore microtubules in PTK cells*, J Cell Biol **118**, 369 (1992).
[6] D. N. Mastronarde, K. L. McDonald, R. Ding, and J. R. McIntosh, *Interpolar spindle microtubules in PTK cells*, J Cell Biol **123**, 1475 (1993).
[7] R. Ding, K. L. McDonald, and J. R. McIntosh, *Three-dimensional reconstruction and analysis of mitotic spindles from the yeast, Schizosaccharomyces pombe*, J Cell Biol **120**, 141 (1993).
[8] D. Pellman, M. Bagget, Y. Tu, G. R. Fink, and H. Tu, *Two microtubule-associated proteins required for anaphase spindle movement in Saccharomyces cerevisiae*, The Journal of cell biology **130**, 1373 (1995).
[9] I. Hagen and M. Yanagida, *Novel potential mitotic motor protein encoded by the fission yeast cut7+*, Nature **347**, 563 (1990).
[10] R. Le Guellec, J. Paris, A. Couturier, C. Roghi, and M. Philippe, *Cloning by differential screening of a Xenopus cDNA that encodes a kinesin-related protein*, Molecular and cellular biology **11**, 3395 (1991).
[11] S. A. Endow, S. Henikoff, and L. Soler-Niedziela, *Mediation of meiotic and early mitotic chromosome segregation in Drosophila by a protein related to kinesin*, Nature **345**, 81 (1990).
[12] H. B. McDonald, R. J. Stewart, and L. S. Goldstein, *The kinesin-like ncd protein of Drosophila is a minus end-directed microtubule motor*, Cell **63**, 1159 (1990).
[13] F. Nédélec, *Computer simulations reveal motor properties generating stable antiparallel microtubule interactions*, The Journal of cell biology **158**, 1005 (2002).
[14] M. Braun, Z. Lansky, G. Fink, F. Ruhnow, S. Diez, and M. E. Janson, *Adaptive braking by Ase1 prevents overlapping microtubules from sliding completely apart*, Nat Cell Biol **13**, 1259 (2011).
[15] Z. Lansky, M. Braun, A. Ludecke, M. Schlierf, P. R. ten Wolde, M. E. Janson, and S. Diez, *Diffusible crosslinkers generate directed forces in microtubule networks*, Cell **160**, 1159 (2015).
[16] D. Johann, D. Goswami, and K. Kruse, *Generation of Stable Overlaps between Antiparallel Filaments*, Phys Rev Lett **115**, 118103 (2015).
[17] E. N. Cytrynbaum, J. M. Scholey, and A. Mogilner, *A force balance model of early spindle pole separation in Drosophila embryos*, Biophys J **84**, 757 (2003).
[18] E. N. Cytrynbaum, P. Sommi, I. Brust-Mascher, J. M. Scholey, and A. Mogilner, *Early spindle assembly in Drosophila embryos: role of a force balance involving cytoskeletal dynamics and nuclear mechanics*, Mol Biol Cell **16**, 4967 (2005).
[19] R. Wollman, G. Civelekoglu-Scholey, J. M. Scholey, and A. Mogilner, *Reverse engineering of force integration during mitosis in the Drosophila embryo*, Mol Syst Biol **4**, 195 (2008).
[20] K. S. Burbank, T. J. Mitchison, and D. S. Fisher, *Slide-and-cluster models for spindle assembly*, Current Biology **17**, 1373 (2007).
[21] R. Loughlin, R. Heald, and F. Nedelec, *A computational model predicts Xenopus meiotic spindle organization*, J Cell Biol **191**, 1239 (2010).

[22] S. B. Reber, J. Baumgart, P. O. Widlund, A. Pozniakovsky, J. Howard, A. A. Hyman, and F. Julicher, *XMAP215 activity sets spindle length by controlling the total mass of spindle microtubules*, Nat Cell Biol **15**, 1116 (2013).
[23] J. Brugues and D. Needleman, *Physical basis of spindle self-organization*, Proc Natl Acad Sci U S A **111**, 18496 (2014).
[24] A. J. Hepperla *et al.*, *Minus-end-directed Kinesin-14 motors align antiparallel microtubules to control metaphase spindle length*, Dev Cell **31**, 61 (2014).
[25] S. Baumgartner and I. M. Tolic, *Astral microtubule pivoting promotes their search for cortical anchor sites during mitosis in budding yeast*, PLoS One **9**, e93781 (2014).
[26] I. Kalinina *et al.*, *Pivoting of microtubules around the spindle pole accelerates kinetochore capture*, Nature cell biology **15**, 82 (2013).
[27] G. Cojoc, A. M. Florescu, A. Krull, A. H. Klemm, N. Pavin, F. Julicher, and I. M. Tolic, *Paired arrangement of kinetochores together with microtubule pivoting and dynamics drive kinetochore capture in meiosis I*, Sci Rep **6**, 25736 (2016).
[28] N. Pavin and I. M. Tolic-Norrelykke, *Swinging a sword: how microtubules search for their targets*, Syst Synth Biol **8**, 179 (2014).
[29] R. Blackwell *et al.*, *Contributions of Microtubule Dynamic Instability and Rotational Diffusion to Kinetochore Capture*, Biophys J **112**, 552 (2017).
[30] R. Blackwell *et al.*, *Physical determinants of bipolar mitotic spindle assembly and stability in fission yeast*, Sci Adv **3**, e1601603 (2017).
[31] F. Ziebert, M. Vershinin, S. P. Gross, and I. S. Aranson, *Collective alignment of polar filaments by molecular motors*, Eur Phys J E Soft Matter **28**, 401 (2009).
[32] See Supplemental Material, which contains references [43-46], for more information, derivations, methods, tables, figures and movies.
[33] J. D. Beinhauer, I. M. Hagan, J. H. Hegemann, and U. Fleig, *Mal3, the fission yeast homologue of the human APC-interacting protein EB-1 is required for microtubule integrity and the maintenance of cell form*, J Cell Biol **139**, 717 (1997).
[34] K. K. Fong, K. K. Sarangapani, E. C. Yusko, M. Riffle, A. Llauro, B. Graczyk, T. N. Davis, and C. L. Asbury, *Direct measurement of microtubule attachment strength to yeast centrosomes*, Mol Biol Cell (2017).
[35] H. A. Kramers, *Brownian motion in a field of force and the diffusion model of chemical reactions*, Physica **7**, 284 (1940).
[36] N. G. Van Kampen, *Stochastic processes in physics and chemistry* (Elsevier, 1992), Vol. 1.
[37] A. Yamashita, M. Sato, A. Fujita, M. Yamamoto, and T. Toda, *The roles of fission yeast ase1 in mitotic cell division, meiotic nuclear oscillation, and cytokinesis checkpoint signaling*, Mol Biol Cell **16**, 1378 (2005).
[38] I. Loiodice, J. Staub, T. G. Setty, N. P. Nguyen, A. Paoletti, and P. T. Tran, *Ase1p organizes antiparallel microtubule arrays during interphase and mitosis in fission yeast*, Mol Biol Cell **16**, 1756 (2005).
[39] J. J. Ward, H. Roque, C. Antony, and F. Nedelec, *Mechanical design principles of a mitotic spindle*, Elife **3**, e03398 (2014).
[40] M. T. Valentine, P. M. Fordyce, and S. M. Block, *Eg5 steps it up!*, Cell Div **1**, 31 (2006).
[41] M. J. Schnitzer, K. Visscher, and S. M. Block, *Force production by single kinesin motors*, Nat Cell Biol **2**, 718 (2000).
[42] E. H. Kellogg, S. Howes, S. C. Ti, E. Ramirez-Aportela, T. M. Kapoor, P. Chacon, and E. Nogales, *Near-atomic cryo-EM structure of PRC1 bound to the microtubule*, Proc Natl Acad Sci U S A **113**, 9430 (2016).

[43] R. Subramanian, E. M. Wilson-Kubalek, C. P. Arthur, M. J. Bick, E. A. Campbell, S. A. Darst, R. A. Milligan, and T. M. Kapoor, *Insights into antiparallel microtubule crosslinking by PRC1, a conserved nonmotor microtubule binding protein*, Cell **142**, 433 (2010).

[44] L. C. Kapitein, M. E. Janson, S. M. van den Wildenberg, C. C. Hoogenraad, C. F. Schmidt, and E. J. Peterman, *Microtubule-driven multimerization recruits ase1p onto overlapping microtubules*, Curr Biol **18**, 1713 (2008).

[45] E. P. Hsu, *Stochastic analysis on manifolds* (American Mathematical Soc., 2002), Vol. 38.

[46] C. W. Gardiner, *Handbook of stochastic methods* (Springer Berlin, 1985), Vol. 4.

[47] J. C. Meadows and J. Millar, *Latrunculin A delays anaphase onset in fission yeast by disrupting an Ase1-independent pathway controlling mitotic spindle stability*, Mol Biol Cell **19**, 3713 (2008).

[48] A. Krull, A. Steinborn, V. Ananthanarayanan, D. Ramunno-Johnson, U. Petersohn, and I. M. Tolic-Norrelykke, *A divide and conquer strategy for the maximum likelihood localization of low intensity objects*, Opt Express **22**, 210 (2014).

FIGURE LEGENDS

FIGURE 1

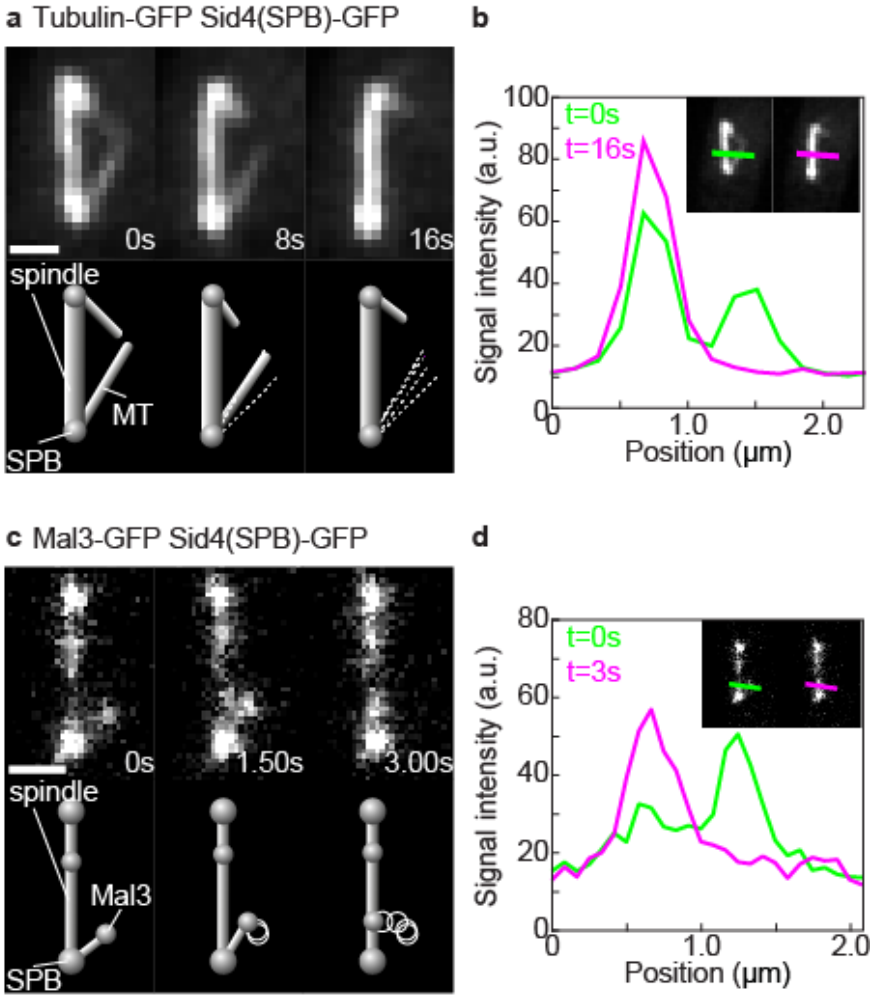

Fig. 1. Formation of MT bundles in *S. pombe* cells. (a) Time-lapse images and the corresponding drawings showing the formation of a parallel MT bundle in an *S. pombe* cell expressing tubulin-GFP and Sid4-GFP. (b), Measurement of the tubulin-GFP signal intensity of MTs before bundling and after bundling (measurement done along the line in the inset with the corresponding color). The measurements were done on the first and the last image in panel a, respectively. (c), Time-lapse images and the corresponding drawings showing the formation of a parallel MT bundle in an *S. pombe* cell expressing Mal3-GFP and Sid4-GFP. (d), Measurements of the Mal3-GFP signal intensity of the spindle and MT before bundling as in b. Scale bars in panels a and c are $1\mu m$.

FIGURE 2

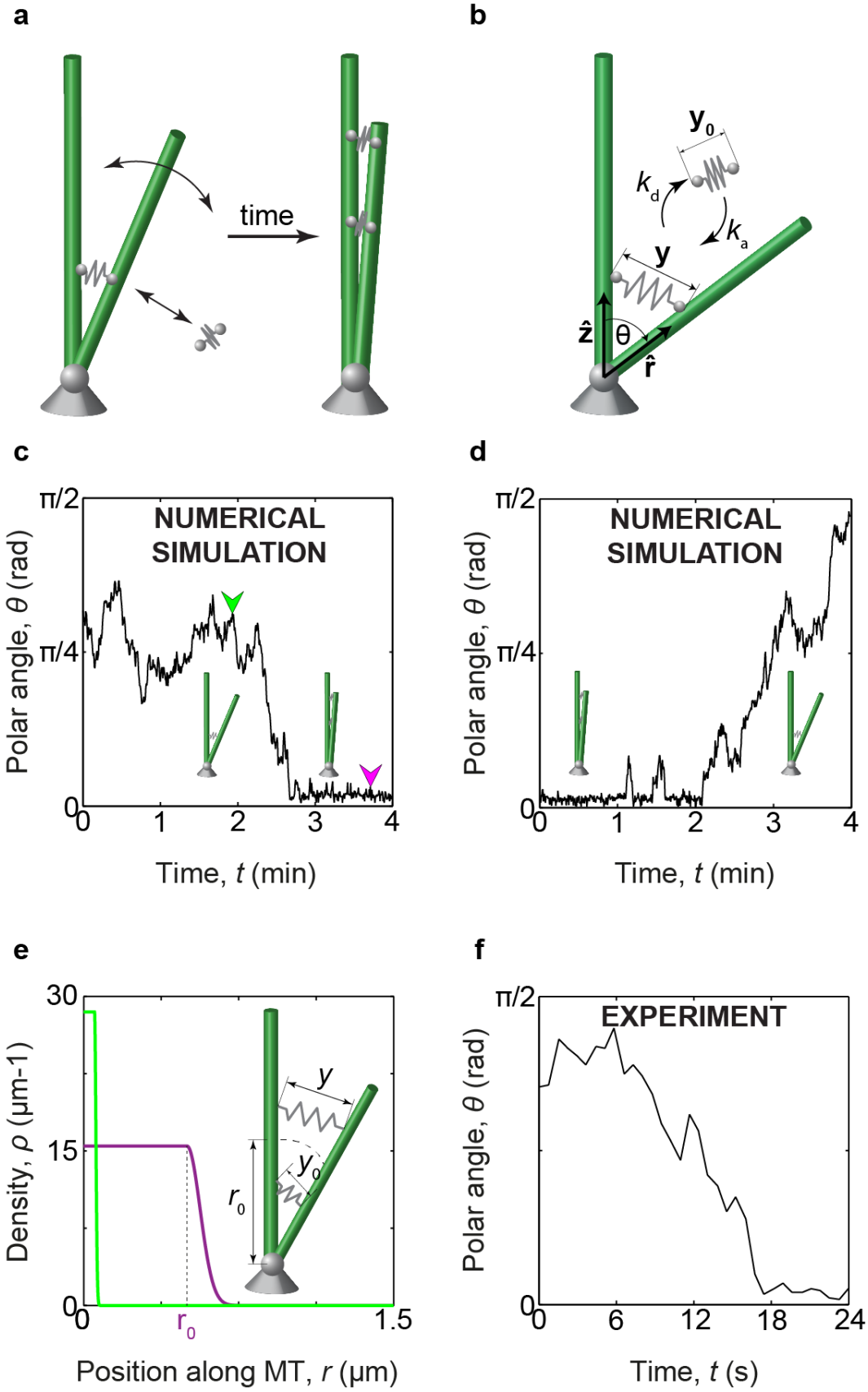
a
time
b
y_0
k_d
k_a
y
$\hat{z}$
θ
$\hat{r}$
c
NUMERICAL SIMULATION
Polar angle, θ (rad)
π/2
π/4
0
0
1
2
3
4
Time, t (min)
d
NUMERICAL SIMULATION
Polar angle, θ (rad)
π/2
π/4
0
0
1
2
3
4
Time, t (min)
e
Density, ρ (μm-1)
30
15
0
0
r_0
1.5
y
y_0
r_0
Position along MT, r (μm)
f
EXPERIMENT
Polar angle, θ (rad)
π/2
0
0
6
12
18
24
Time, t (s)

Fig. 2. Scheme of the model and numerical solutions. (a), Cartoon representation of the bundling process. A MT (green rod) pivots around the spindle pole body (grey ball). Cross-linking proteins (grey springs) attach and cause the MTs to from a bundle. (b), Scheme of the model. The orientations of two MTs are represented by the unit vectors $\hat{\mathbf{r}}$ and $\hat{\mathbf{z}}$. Cross-linking proteins attach to and detach from MTs at rates k_{a} and k_{d}, respectively. The elongation of the attached cross-linking protein is denoted y and their relaxed length is y_0. The angle between the MTs is denoted θ. (c), A sample path for the starting angle $\theta = 0.9\ \mathrm{rad}$, which shows a bundling event. (d), A sample path for an unbundling event. (e), Cross-linking protein density profiles along the MT for two points on the path shown in c, denoted by arrowheads in corresponding colors (large image). The point r_0 is shown for the magenta line. The inset shows a schematic of the orientations of attached cross-linkers. The cross-linkers attached within the distance r_0 from the spindle pole body are always relaxed, while those attached at larger distances from the spindle pole body are elongated. (f), A sample of MT angle time series obtained using light microscopy on cells with the Mal3-GFP label. All calculations are done with $c_0 = 300\ \mu\mathrm{m}^{-1}$, $R = 1.5\ \mu\mathrm{m}$, $D = 0.001\ \mathrm{rad}^2\mathrm{s}^{-1}$, other parameters shown in Table 1.

FIGURE 3

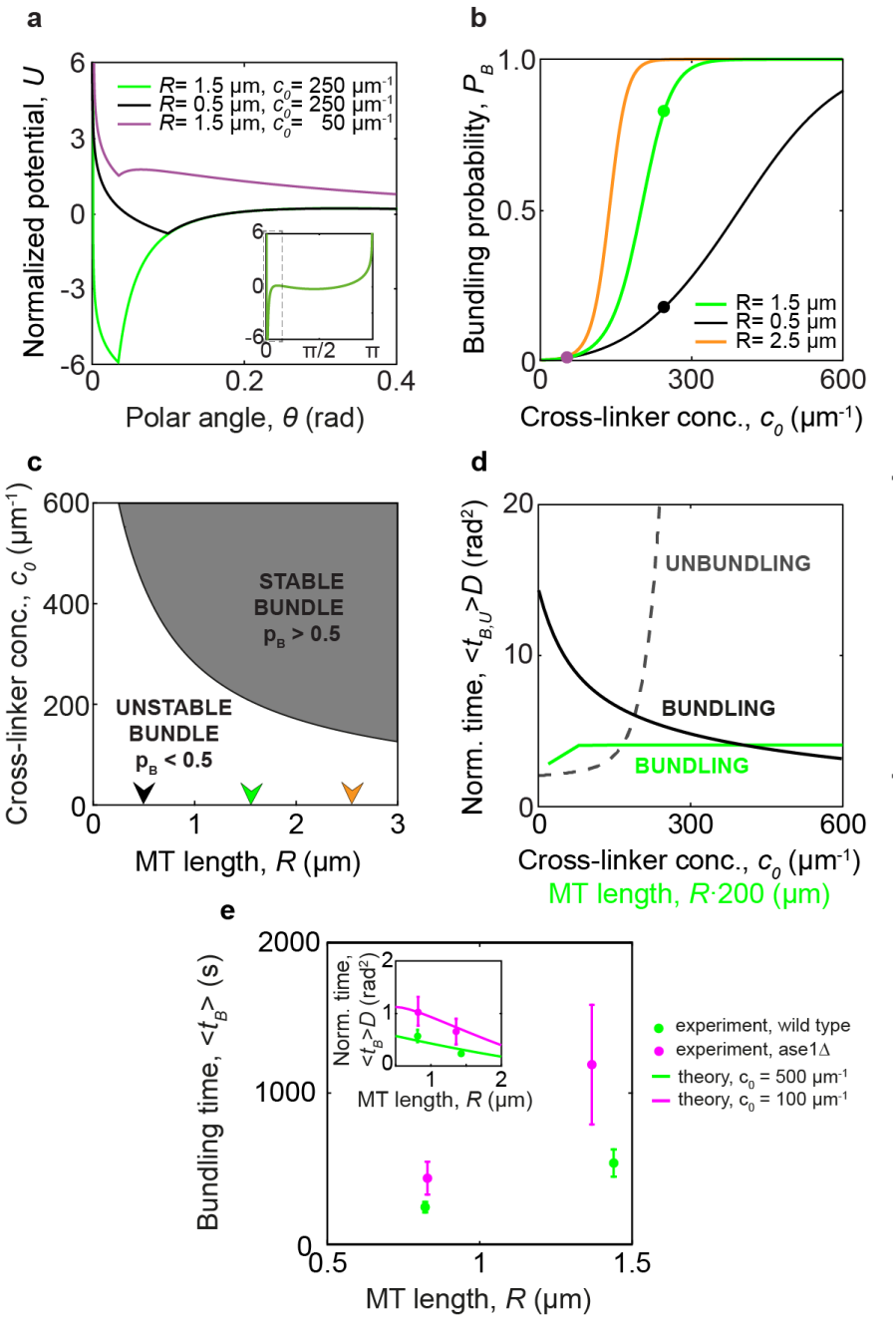

Fig. 3. Solutions of the model in the adiabatic approximation. (a), The effective potential as a function of the polar angle for small angles. The inset shows the potential for all angles. (b), Bundling probability as a function of c_0 for three different values of R. The colors of the dots correspond to the color code of the parameters used in a. (c), Phase diagram. The gray area represents the region where bundles are stable. The arrowheads represent the values of R used in b. (d), Normalized bundling and unbundling times. The black lines represent the normalized bundling (solid line) and unbundling time (dashed line) as a function of c_0 for $R = 1.5\ \mu\text{m}$. The green line represents the normalized bundling time as a function of R for

$c_0 = 250\ \mu\text{m}^{-1}$. (e) Experimentally measured bundling times for wild type (green) and *ase*1Δ cells (magenta). Inset shows the comparison between measured normalized bundling time (dots with error bars) and theoretical curves for $c_0 = 500\ \mu\text{m}^{-1}$ (solid green line) and $c_0 = 100\ \mu\text{m}^{-1}$ (solid magenta line).

Table 1. Values of the constant parameters used in this paper.

Parameter	Value	Source
k	0.1 pNnm^{-1}	Value for Eg5 (ref. [16,40])
f_c	3 pN	Value for kinesin-1 (ref. [41])
y_0	40 nm	Value for Prc1 (ref. [42,43])
D_m	0.05 μm^{2}s^{-1}	Value for Ase1 (ref. [15,44])
k_a	0.01 s^{-1}	Value for Ase1(ref. [15])
k_{d0}	0.1 s^{-1}	Value for Ase1 (ref. [15])

Author contributions and acknowledgements

N.P. and I.T. designed and supervised the project. M.P. and N.P. developed the theory. L.W. carried out the experiments and A.M. analyzed the experimental data. N.P., M.P. and I.T wrote the manuscript with input from L.W. and A.M. The data that support the findings of this study are available from the corresponding authors upon reasonable request. Contact N.P. for information on the theory presented and I.M.T with requests related to the experimental measurements.

We thank D. Radić and V. Despoja for comments on the manuscript and M. Glunčić for valuable discussions and advice regarding our theoretical model; F. Elsner from the Electronics Service of MPI-CBG for building the thermoelectric device; J. Millar for yeast strains; Light Microscopy Facility of MPI-CBG for help with microscopy; J. Brugués, T.M. Franzmann, A. Garcia Ulloa and the rest of the Tolić lab for discussion and advice; and I. Šarić for editing the figures. We acknowledge the Unity through Knowledge Fund (UKF), German Research Foundation (DFG), European Research Council (ERC) and the QuantiXLie Center of Excellence for funding.

FIGURE 1

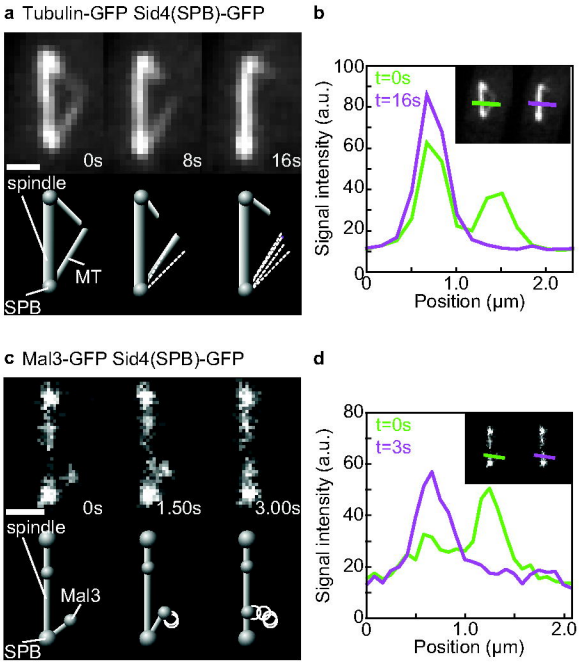
a Tubulin-GFP Sid4(SPB)-GFP
0s
8s
16s
spindle
MT
SPB
b
t=0s
t=16s
Signal intensity (a.u.)
Position (μm)
c Mal3-GFP Sid4(SPB)-GFP
0s
1.50s
3.00s
spindle
Mal3
SPB
d
t=0s
t=3s
Signal intensity (a.u.)
Position (μm)

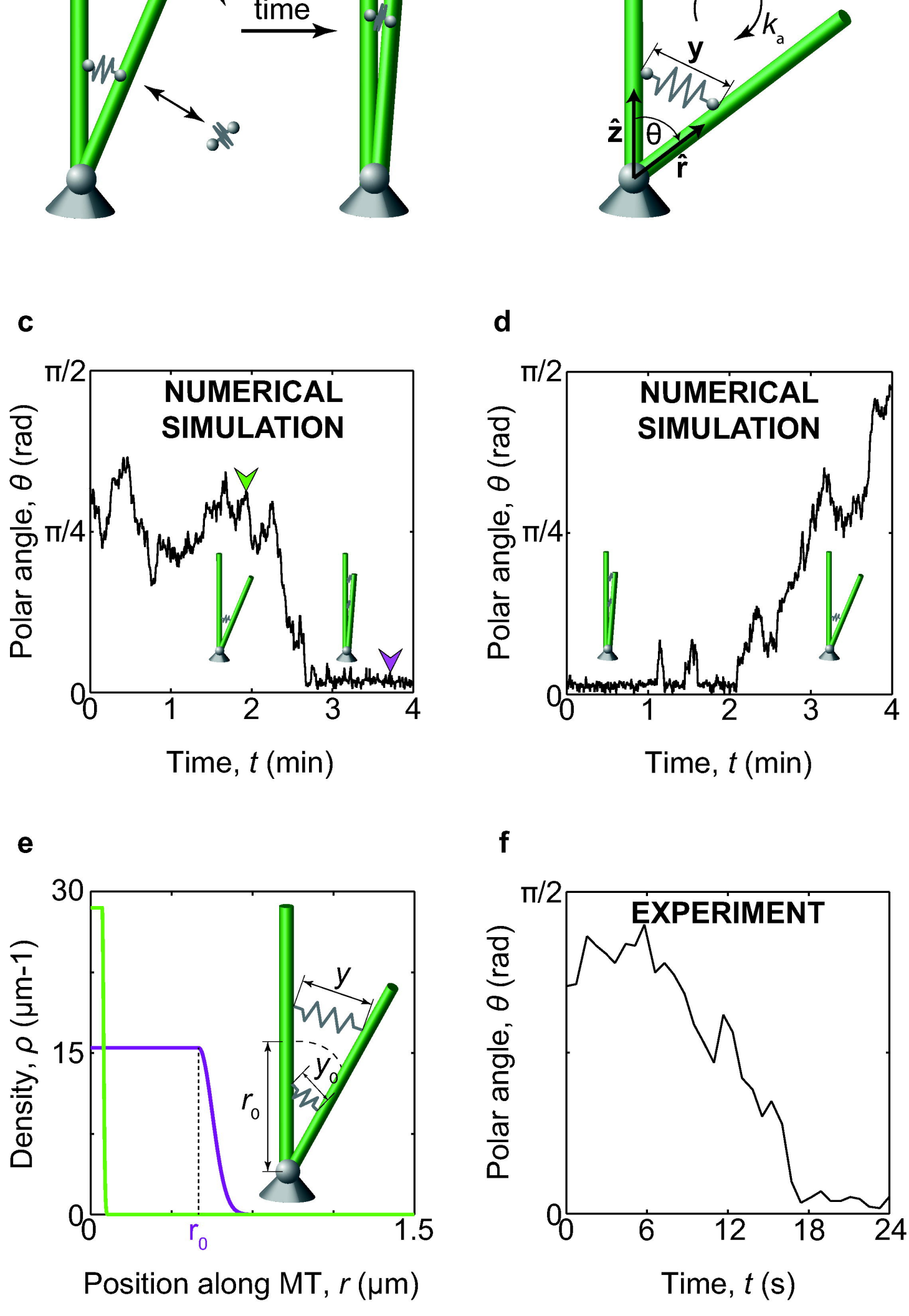
time
k_a
y
$\hat{z}$
θ
$\hat{r}$
c
NUMERICAL SIMULATION
Polar angle, θ (rad)
π/2
π/4
0
0
1
2
3
4
Time, t (min)
d
NUMERICAL SIMULATION
Polar angle, θ (rad)
π/2
π/4
0
0
1
2
3
4
Time, t (min)
e
Density, ρ (μm-1)
30
15
0
0
r_0
1.5
y
y_0
r_0
Position along MT, r (μm)
f
EXPERIMENT
Polar angle, θ (rad)
π/2
0
0
6
12
18
24
Time, t (s)

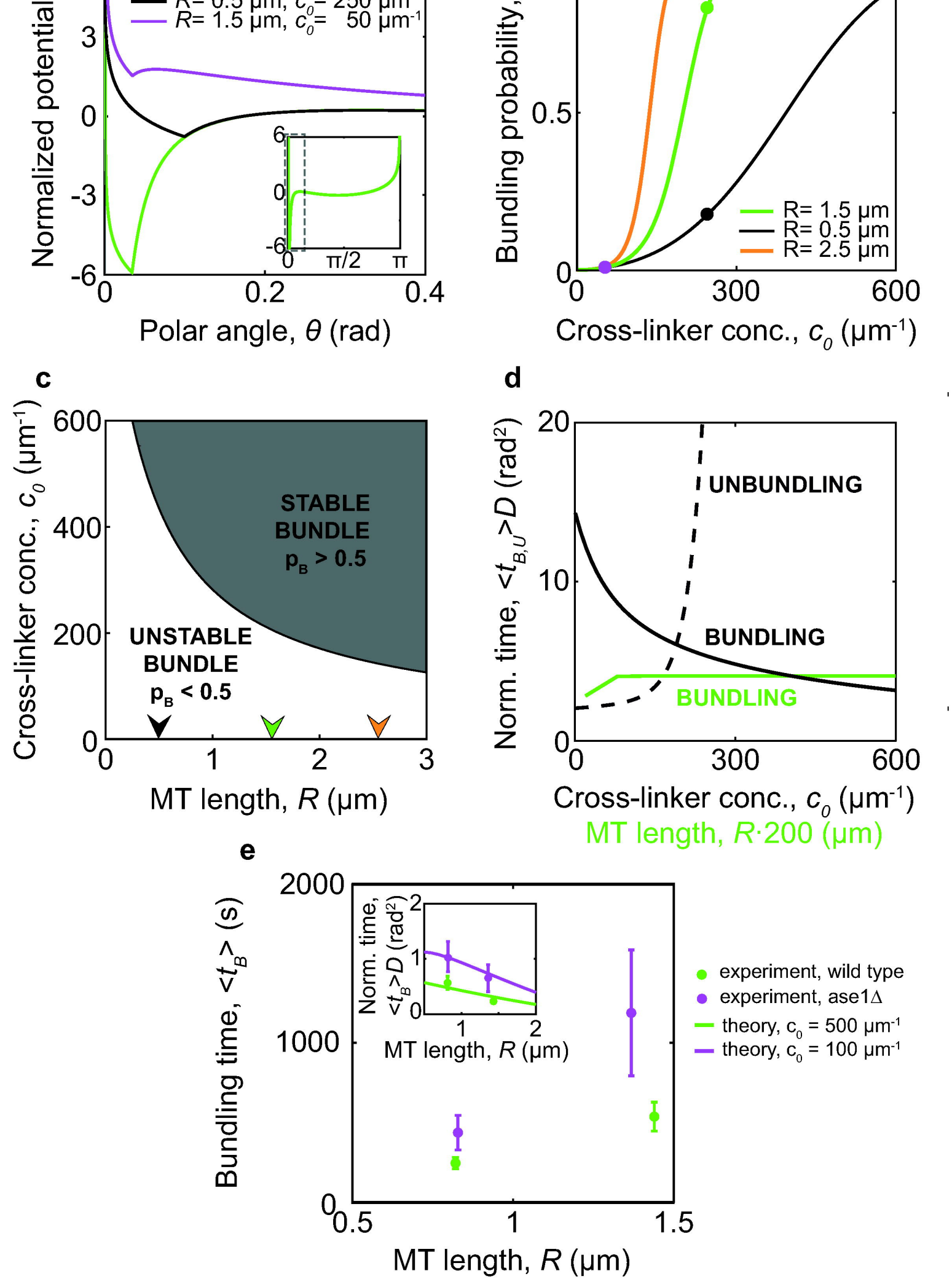
Normalized potential
R= 1.5 μm, c0= 50 μm-1
Polar angle, θ (rad)
Bundling probability
R= 1.5 μm
R= 0.5 μm
R= 2.5 μm
Cross-linker conc., c0 (μm-1)
c
Cross-linker conc., c0 (μm-1)
STABLE BUNDLE pB > 0.5
UNSTABLE BUNDLE pB < 0.5
MT length, R (μm)
d
Norm. time, <tB,U>D (rad2)
UNBUNDLING
BUNDLING
BUNDLING
Cross-linker conc., c0 (μm-1)
MT length, R·200 (μm)
e
Bundling time, <tB> (s)
Norm. time, <tB>D (rad2)
MT length, R (μm)
experiment, wild type
experiment, ase1Δ
theory, c0 = 500 μm-1
theory, c0 = 100 μm-1
MT length, R (μm)